Compensation of Hyperspectral Data for Atmospheric Effects

Michael K. Griffin and Hsiao-hua K. Burke

Hyperspectral imaging sensors are used to detect and identify diverse surface materials, topographical features, and geological features. Because the intervening atmosphere poses an obstacle to the retrieval of surface reflectance data, algorithms exist to compensate the measured signal for the effects of the atmosphere. This article provides an overview and an evaluation of available atmospheric compensation algorithms for the visible-through-shortwave infrared spectral region, including comparison of operational characteristics, input requirements, algorithm limitations, and computational requirements. Statistical models based on empirical in-scene data are contrasted with physics-based radiative transfer algorithms. The statistical models rely on *a priori* scene information that is coupled with the sensor spectral observations in a regression algorithm. The physics-based models utilize physical characteristics of the atmosphere to derive water vapor, aerosol, and mixed gas contributions to the atmospheric signal. Treatment of aerosols in atmospheric compensation models varies considerably and is discussed in some detail. A three-band ratio approach is generally used for the retrieval of atmospheric water vapor. For the surfaces tested in this study, the retrieved surface reflectances from the two physics-based algorithms are similar under dry, clear conditions but differ under moist, hazy conditions. Sensitivity of surface-reflectance retrievals to variations in scene characteristics such as the solar zenith angle, atmospheric visibility, aerosol type, and the atmospheric temperature profile is presented in an effort to quantify the limitations of the models.

Hyperspectral imaging sensors have been used for more than a decade to help detect and identify diverse surface materials, topographical features, and geological features. Hyperspectral data are not immune, however, to the effects of the intervening atmosphere. Atmospheric compensation refers to the removal of unwanted atmospheric components of the measured radiance. For hyperspectral data analysis, the general objective of atmospheric compensation algorithms is to remove solar illumination and atmospheric effects (predominantly aerosol scattering and water vapor absorption) from the measured spectral data so that an accurate estimate of the surface reflectance can be obtained. The retrieved surface-reflectance spectra can then be compared with a library collection of spectra representing various materials.

Hyperspectral reflectance measurements of the solar and near-infrared reflectance spectrum satisfy a host of scientific research applications, including estimating atmospheric water vapor, cloud properties and aerosols, agriculture and forest properties, mineralogy, soil type, snow and ice hydrology, biomass burning, environmental hazards, calibration of aircraft and satellite sensors, sensor simulation and validation, radiative transfer modeling, and atmospheric compensation. Figure 1 depicts the relationship between spectral measurement and various features to be retrieved. As shown in the figure, the contiguous narrowband character of hyperspectral measurements provides a unique source of information for a wide variety of research areas, such as geological, ecological, and oceanographic endeavors.

Although numerous airborne hyperspectral platforms exist, two platforms have been used extensively in this study and are described in the section that follows. Using the data from these platforms, we can take several different approaches to obtain an accurate estimation of the surface reflectance; a description and comparison of the more popular techniques for atmospheric compensation is presented. Requirements for atmospheric compensation of hyperspectral data include the ability to account for stressing atmospheric conditions (e.g., high moisture, heavy aerosol/particulate loading, partial cloud cover, low sun angle) as well as clear sky. Changing the inputs to the compensation model can significantly affect the retrieved surface reflectance. The sensitivity of the retrieved reflectance to controlled variations in the model input parameters is analyzed and discussed. Lastly, the computational burden, an important consideration for physics-based models, is estimated for two of the models.

Hyperspectral Data Sources

To meet the requirements for a number of scientific applications, airborne imaging spectrometers were designed to achieve substantial improvements over existing multispectral imaging systems in the areas of spatial resolution, sensitivity, and accuracy of absolute calibration. The Airborne Visible Infrared Imaging Spectrometer (AVIRIS) sensor has been used extensively to provide hyperspectral measurements in the visible, near-infrared, and shortwave infrared (SWIR) spectra [1]. AVIRIS contains 224 different detectors, each with a spectral bandwidth of approximately 0.010 μm, allowing it to cover contiguously the entire spectral range from 0.38 to 2.5 μm. AVIRIS uses a

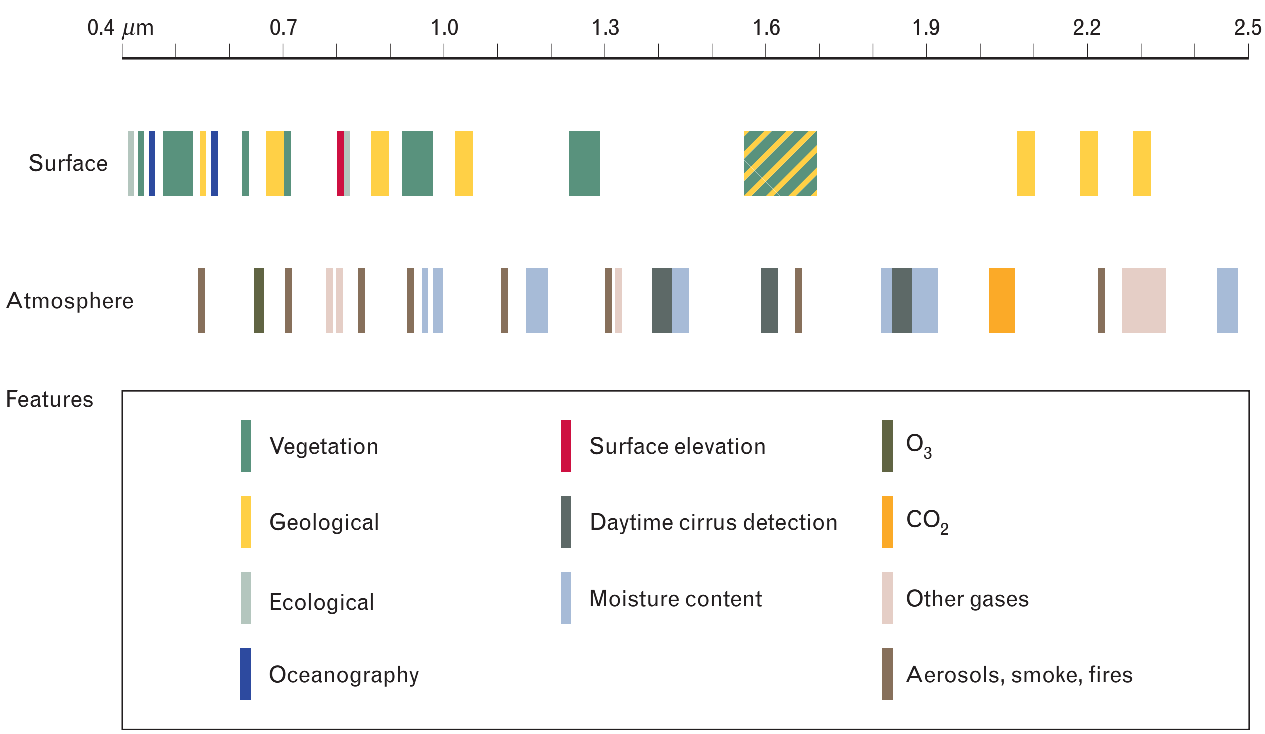

FIGURE 1. The locations of spectral regions in the visible, near infrared, and shortwave infrared, which are used to retrieve the features listed.

scanning mirror to sweep back and forth in a whisk-broom fashion, resulting in 614 pixels for each scan line. Each pixel covers a 20-m × 20-m-square area on the ground (with some overlap between pixels), yielding a ground swath width of approximately 11 km for an ER-2 aircraft flight altitude of 20 km. More recently, AVIRIS has been mounted on a low-flying (~3 to 5 km) aircraft that provides higher spatial-resolution imagery and smaller swaths [2].

The Hyperspectral Digital Imagery Collection Experiment (HYDICE) sensor is a push-broom imaging spectrometer that uses a bi-prism dispersing element and a two-dimensional focal-plane array (FPA) to enable a single optical path design [3, 4]. The FPA is a 320-element by 210-detector indium antimonide (InSb) array that supports operations over the full 0.4-to-2.5-μm spectral range. Mounted on a CV 580 aircraft, HYDICE has an operating altitude range of 1.5 to 8 km and spatial resolutions of 0.8 to 4 m. At the lowest flight altitude, the HYDICE swath width is on the order of 270 m. Calibration is done in-flight through the full optical system, and is referenced to a National Institute of Standards and Technology (NIST) ground standard.

Atmospheric Properties

The effects of the intervening atmosphere must be considered to estimate the underlying surface reflectance from a remote airborne platform. Typically, at wavelengths below 2.5 μm, the incident solar flux is impacted by (1) the absorption by well-mixed gases such as ozone (O_3), oxygen (O_2), methane (CH_4), and carbon dioxide (CO_2); (2) absorption by water vapor; (3) scattering by molecules; and (4) scattering and absorption by aerosols and hydrometeors. Gas-absorption effects vary strongly with wavelength and gas properties, and can have a significant impact on the received solar flux. Aerosol absorption, on the other hand, is relatively minor compared to molecular absorption, and is generally viewed as a smoothly varying continuous function. Typical absorption loss due to aerosols is limited to a few percent, with minimum absorption occurring for maritime aerosols and maximum absorption found in urban aerosols that tend to contain significant amounts of carbon. Scattering from both molecules in the visible/near infrared (VNIR) and aerosols in the VNIR/SWIR is also found to vary slowly and continuously with wavelength. The largest scattering effects are observed in the visible with decreased effects at longer wavelengths. Molecular scattering effects are significant out to 0.75 μm, while aerosol scattering continues to have an impact at SWIR wavelengths (1.3 μm), predominantly due to the larger aerosol particle size, which can reach 1 μm. Under cloud-free conditions, which are usually desired for experimental hyperspectral data collections, aerosols provide the bulk of the solar scattering, while molecular (Rayleigh) scattering can be important at visible wavelengths. Models have been developed on the basis of the size and near-spherical shape of aerosols to estimate the effects of scattering on the incident solar flux [5]. Scattering by molecules can be defined by the well-known Rayleigh scattering theorem [6].

Mixed gases, while making a smaller and discontinuous contribution to the transmittance spectrum, can be modeled accurately and play an important role in the retrieval of specific properties of the earth-atmosphere system [7]. Figure 2 shows the atmospheric transmittance for a number of important gaseous absorption features observed in the spectral region from 0.4 to 2.5 μm for two atmospheric conditions: dry and clear, or humid and hazy. Weak ozone absorption is present from 0.5 to 0.7 μm. At 0.76 μm, a strong, narrow oxygen absorption line is present; a weaker oxygen line is located at 1.27 μm. CO_2 absorbs strongly from 1.9 to 2.1 μm. The effect of the CO_2 absorption is partially negated by a strong overlapping water vapor absorption band. CO_2 also exhibits a weak absorption line at 1.43 μm. Weak absorption by methane (CH_4)is present from 2.2 to 2.5 μm.

Water vapor absorption in the VNIR spectrum is characterized by a number of bands of various strengths and spectral widths. Two very weak absorption bands are located at 0.6 and 0.66 μm. Slightly stronger and more significant bands are located at 0.73, 0.82, and 0.91 μm. At 0.94 and 1.14 μm, water vapor absorption is strong enough that measurements at the band centers and off-center locations can be used to derive the total column water vapor [8–10]. Water vapor absorption near 1.375, 1.9 and 2.5 μm is strong enough to make retrieval of the surface reflec-

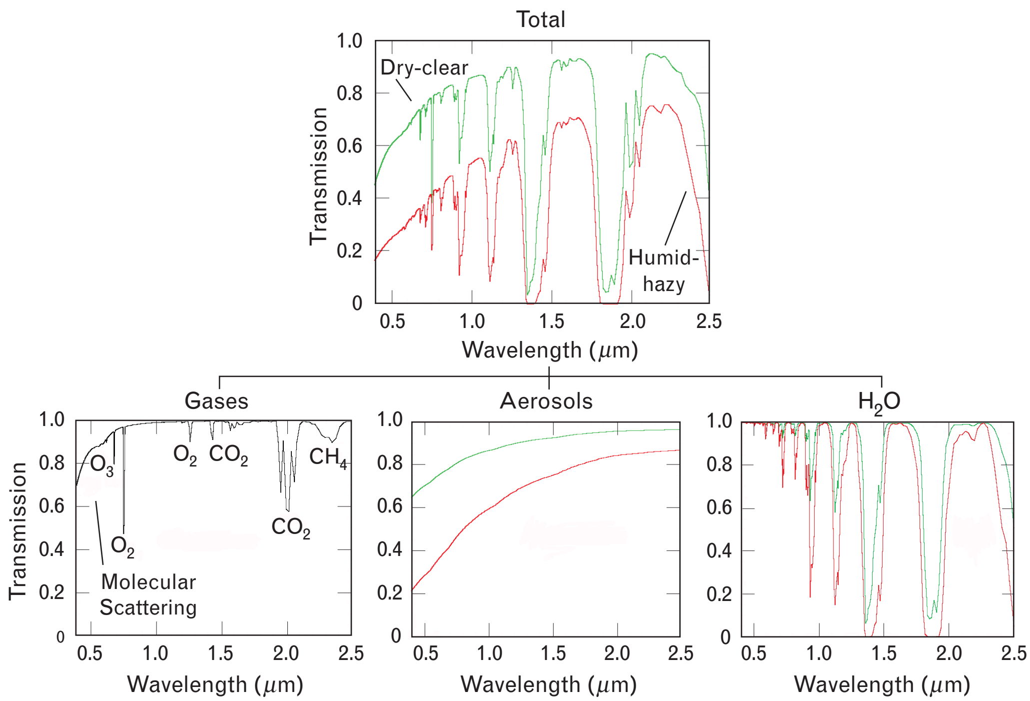

FIGURE 2. Atmospheric transmission plotted for two conditions (dry-clear in green and humid-hazy in red). The contributions to the overall transmission by mixed gases, aerosols, and water vapor are shown in separate plots for the same spectral range.

tance difficult or impossible. Therefore, these bands are used to obtain information about high-altitude moisture and cloud effects [11], since much of the signal at these wavelengths comes from the mid-to-upper troposphere. The large number of strongly absorbing water vapor bands makes the adjustment for water vapor a significant focus of atmospheric compensation routines.

While water vapor clearly has the largest effect on the transmittance, aerosols play an important role and must be handled properly by compensation routines if an accurate estimate of the surface reflection is to be obtained. Aerosol effects can vary widely with atmospheric moisture, aerosol type, or makeup and optical depth or visibility [5].

The application of atmospheric compensation to retrieve surface reflectance can also lead to better characterization of the atmosphere. Secondary products of the physics-based atmospheric compensation approaches can include a map of the integrated column water vapor and scene aerosol type and visibility. The spectral information itself can be used to provide quantitative information about atmospheric features such as clouds, dust, or smoke [12]. For an example of how spectral information is used to characterize a hyperspectral image, see the sidebar entitled "Characterization of a Hyperspectral Image."

Atmospheric Compensation Models

Imaging spectrometers acquire images in an array of contiguous spectral bands such that a complete set of reflectance or emittance spectra is measured for each pixel in the image. The two spatial image dimensions (elements and lines) are combined with the spectral dimension to produce the hyperspectral image cube. Typical reflectance measurements from hyperspectral sensors contain information not only about the spectral characteristics of the surface but of the intervening atmosphere as well. Because these sensors are primarily used as a tool to derive spectral-reflectance information for the earth's surface, it is advantageous to be able to remove, or compensate for, the effects of the intervening atmosphere. Figure 3 shows an example of the uncompensated, or at-sensor, radiance

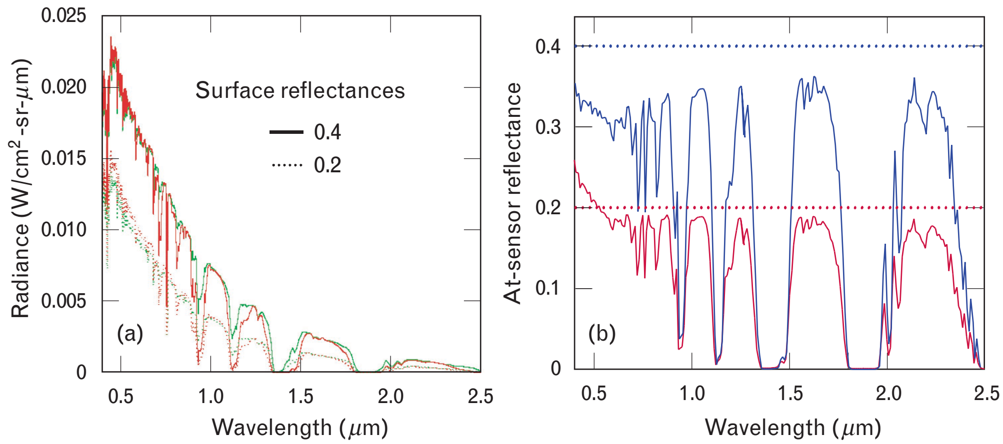

FIGURE 3. Plots of (a) simulated radiance as measured by a hyperspectral sensor and (b) at-sensor reflectance (solid lines) for two values of a spectrally uniform surface reflectance of 0.2 and 0.4. Simulated radiances are shown for a solar zenith angle of 30° and for two atmospheric compositions: hazy and humid (red lines) and clear and dry (green lines). At-sensor reflectances are shown for the hazy and humid case only, for which dotted lines represent the surface reflectance used in the simulations.

and reflectance spectra (radiance normalized by the incident solar flux) for simulated hyperspectral measurements of scenes with a spectrally uniform surface reflectance. The radiance (Figure 3[a]) was computed for two different atmospheric compositions: humid and hazy, and dry and clear, for two uniform surface-reflectance values (0.2 and 0.4). Differences in the two cases are most noticeable in the absorption bands where the measured radiance is strongly affected by the moisture content of the atmosphere. The reflectance spectra (Figure 3[b]) display similar features throughout the VNIR region. It is clear that the effects of specific atmospheric constituents, such as water vapor and aerosol particles, can mask the true nature of a remotely sensed surface.

Various types of atmospheric compensation models exist for application to hyperspectral data. Most fall into two basic categories: statistical or empirical, and physics based. The former use *a priori* knowledge of the reflectance characteristics of specific reference objects (such as calibration panels) in a scene to develop statistical relationships between the at-sensor observations and the surface reflectance. The empirical line method (ELM) is a commonly used statistics-based atmospheric compensation model [13, 14]. The ELM creates a linear-regression equation for each spectral band that provides a relationship between the raw radiance and the surface reflectance. This process is equivalent to removing the solar radiance and the atmospheric path radiance from the measured signal. Gain and offset factors for each spectral band derived from this relationship are applied to all other pixels in the scene to remove the atmospheric component from the measurements. The ELM provides good estimates of the surface reflectance, assuming that the reference-object spectral reflectances are accurately known. However, information pertaining to the intervening atmosphere is not derived with this type of approach, and ELM does not properly account for topographic variations in the atmospheric path, which can result in elevation-dependent residual atmospheric absorptions.

Other statistical techniques are used to adjust or normalize the raw radiance data. These techniques tend to be more of a calibration tool than a compensation method. Two such techniques are the internal average relative reflectance (IARR) [15] and the flat field correction (FFC) [13]. The IARR acts to normalize images to a scene-average spectrum, which is particularly effective for reducing hyperspectral data to relative reflectance in an area where no ground measurements exist and little is known about the

CHARACTERIZATION OF A HYPERSPECTRAL IMAGE

TYPICAL MEASUREMENTS from hyperspectral sensors contain information not only about the spectral characteristics of the surface but of the intervening atmosphere as well. The imagery shown in Figure A is from the AVIRIS sensor, where the measured radiance has been converted to at-sensor reflectance by dividing by the incident solar irradiance corrected for sun angle and earth-sun distance. The scene was collected in the foothills east of Linden, California, on 20 August 1992 and consists of a forest fire emitting a thick plume of smoke toward the east (north is toward the top of the image). A cloud produced by the strong thermal properties of the fire overlies the smoke plume. Toward the northwest, two smoldering fires emit a thin veil of smoke that covers much of the upper half of the scene. The southwest portion of the scene is free of clouds and smoke. Shadows are also observed just to the north of the cloud. The left image was generated via a natural color rendition by using three bands in the visible portion of the spectrum (red: 0.65 μm, green: 0.55 μm, blue: 0.45 μm). The right image is formed by using visible and shortwave-infrared bands (red: 2.14 μm, green: 1.62 μm, blue: 0.55 μm). While the left image displays the visible characteristics of the scene, the right image emphasizes features present in longer wavelengths, where the atmosphere is more transparent to smoke. The dark brown patch of burnt vegetation in the region of the smoke from the smoldering fires and the bright red and yellow colors depicting the location of the fire hot spots are visible. The radiance measured near the fires is due to a combination of reflected solar and emitted thermal radiance (from the intense heat of the fire) that is most pronounced in the shortwave-infrared bands.

Figure B shows a number of spectral features that are prominent in these images. Regions of moderate to strong water vapor absorption are found where the observed reflectance is low. High

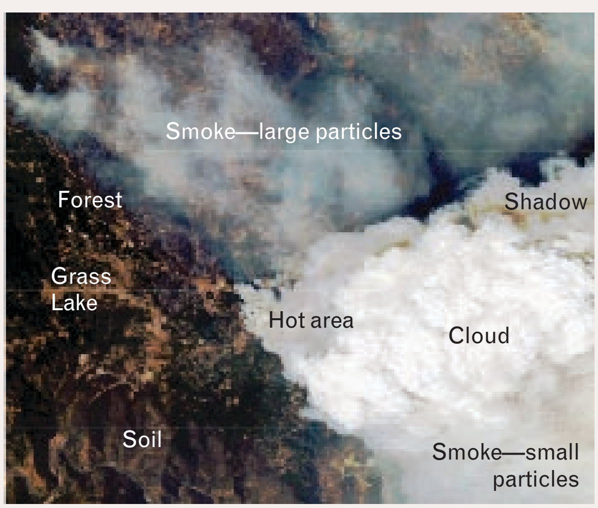

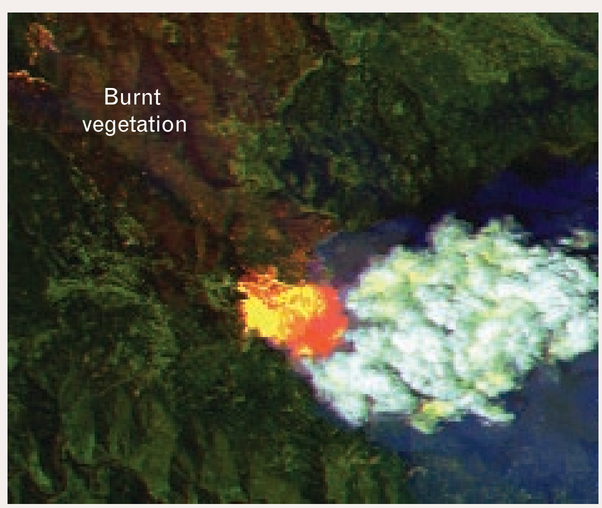

FIGURE A. AVIRIS sensor red-green-blue (RGB) imagery of a scene collected in the foothills near Linden, California. The left image is a pseudo-natural color depiction. The right image is a false-color display emphasizing details visible at shortwave-infrared band signatures.

reflectance features such as clouds, the thick smoke plume, and highly reflective vegetation in the near infrared have prominent spectral signatures. Note that while clouds exhibit high spectral reflectance across all wavelengths, the reflectance of the thick smoke plume decreases dramatically beyond the first strong water vapor absorption band (1.37 μm). Also note the reflectance difference between the smoke (large particles) that overlays burnt vegetation and the undisturbed forest vegetation in the near infrared, and to a greater extent in the shortwave infrared.

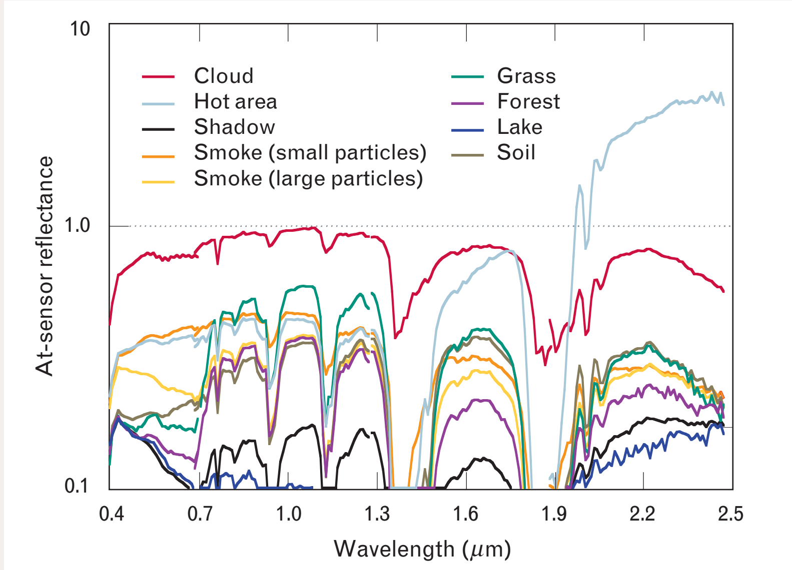

FIGURE B. Spectral curves for nine features identified in the AVIRIS sensor imagery of Figure A.

scene. It works best for arid areas with no vegetation. An average spectrum calculated from the entire scene is used as the reference spectrum, which is divided into the spectrum at each pixel of the image. The FFC works similarly, normalizing the hyperspectral data to an area of known flat reflectance, and again reducing the hyperspectral data to relative reflectance.

When true atmospheric compensation is desired and direct information about a scene is unknown, statistical algorithms may not be applicable. For these cases, a more robust algorithm is needed to retrieve the surface characteristics. Typically, physics-based models are chosen for this task. Two of the more commonly used models are Atmospheric Removal (ATREM) [16] and Fast Line-of-Sight Atmospheric Analysis of Spectral Hypercubes (FLAASH) [17]. While ATREM and FLAASH apply different methods of atmospheric compensation, both use variations of the three-band ratio techniques [8, 9] to account for the effects of water vapor on the hyperspectral measurements. The methodology of the three-band ratio technique and the model implementation differences are described in more detail in a later section.

Atmospheric Compensation Theory

For physics-based models, the relationship between the surface reflectance ρ_s and the at-sensor reflectance ρ^* can be represented by the following equation:

$$\rho^* = \rho_a T_g + \left(\frac{\rho_s T_g T^{\downarrow} T^{\uparrow}}{1-\rho_{adj} S} + \frac{\left(\rho_{adj} - \rho_s\right) T_g T^{\downarrow} T^{\uparrow}}{1-\rho_{adj} S} r \right), \quad (1)$$

where T_g is the gaseous transmittance, ρ_a is the atmospheric reflectance, $T^{\downarrow}$ and $T^{\uparrow}$ are the upward and downward scattering transmittances, r is the diffuse-to-total transmittance ratio for the ground-sensor path, and S is the spherical albedo of the atmosphere. The parameter ρ_{adj} represents the surface reflectance averaged over a region around the pixel to account for scattering into the pixel-to-sensor path, known as the adjacency effect. While FLAASH has the option of performing adjacency calculations, ATREM does not incorporate scattering from adjacent pixels into its computations. In ATREM, a simplification to Equation 1 is made of the form $\rho_{adj} = \rho_s$. Using this ap-

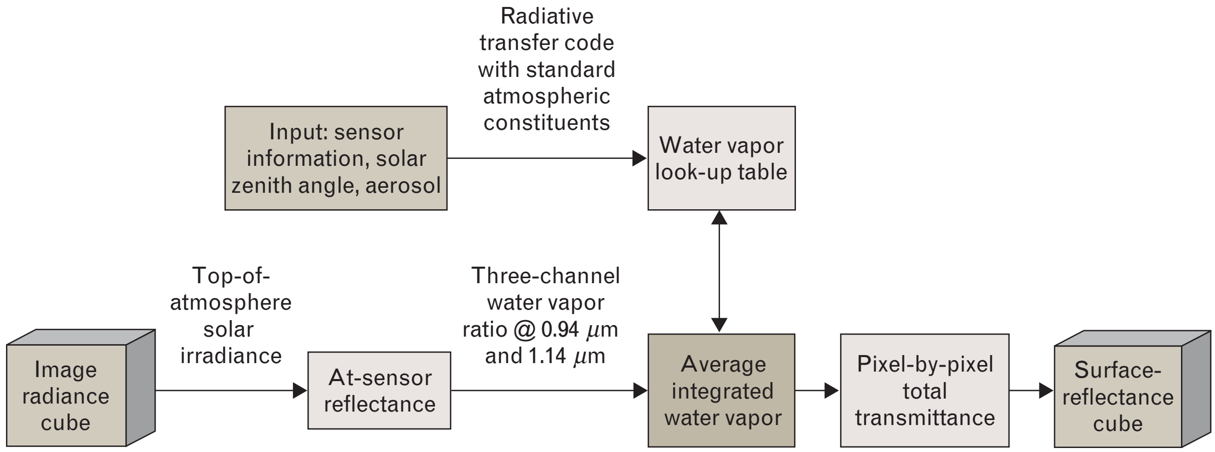

FIGURE 4. Schematic flow of the physics-based Atmospheric Removal (ATREM) program. The diagram shows the various steps used to convert the radiance data to surface-reflectance data.

proximation, and given a measured radiance spectrum, we can derive the at-sensor reflectance from the sensor radiance and then compute the surface reflectance from the following equation:

$$\rho^* = \frac{\left(\dfrac{\rho^*}{T_g} - \rho_a\right)}{T^{\downarrow}T^{\uparrow} + S\left(\dfrac{\rho^*}{T_g} - \rho_a\right)} . \tag{2}$$

Figure 4 shows the schematic flow of the ATREM program. ATREM uses a narrowband spectral model [7] to derive the gaseous transmittance and the Second Simulation of the Satellite Signal in the Solar Spectrum (6S) code [18] to compute the necessary scattering terms by using a user-selected aerosol model. The individual gas concentrations are assumed to be uniform across the scene except for water vapor, which the algorithm treats separately. In this manner, only a single scene transmittance spectrum is calculated for each uniform gas. Water vapor transmittances, however, are calculated on a pixel-by-pixel basis. ATREM provides a simple input parameter interface and relatively fast execution. Input parameters are limited to basic atmospheric parameters (aerosol visibility and model type, atmospheric model, and ozone concentration) and solar and viewing geometry. The model processes both AVIRIS and HYDICE spectral hypercubes and has features for processing hyperspectral data cubes from other sensors such as Hyperion.

FLAASH [17] utilizes the full Moderate Resolution Transmittance (MODTRAN)* radiative-transfer code [19] functionality, which includes a complete package of transmittance and scattering methods, including a full accounting for adjacency effects (the scattering from adjacent pixels into the current pixel-sensor line of sight) associated with atmospheric scattering. Figure 5 shows the schematic flow of the FLAASH code. FLAASH has multiple spectral resolution options to increase processing speed. In addition to retrieving the surface reflectance and the column water vapor amount (for each pixel in a scene), it also offers the options of retrieving the aerosol optical depth (using a dark-pixel approach) and the terrain elevation (using the 0.76-μm O_2 line), and of masking out clouds. The technique used by FLAASH to derive the surface spectral reflectance, which includes the adjacency contribution, employs Equation 1.

Model Comparisons

For all atmospheric compensation models, the primary output product is the surface reflectance. For physics-based models to derive an accurate estimate of the surface reflectance, the effects of aerosols, water vapor, and other mixed gases must be taken into ac-

* Throughout this article, all mentions of MODTRAN refer to version 4 of the software.

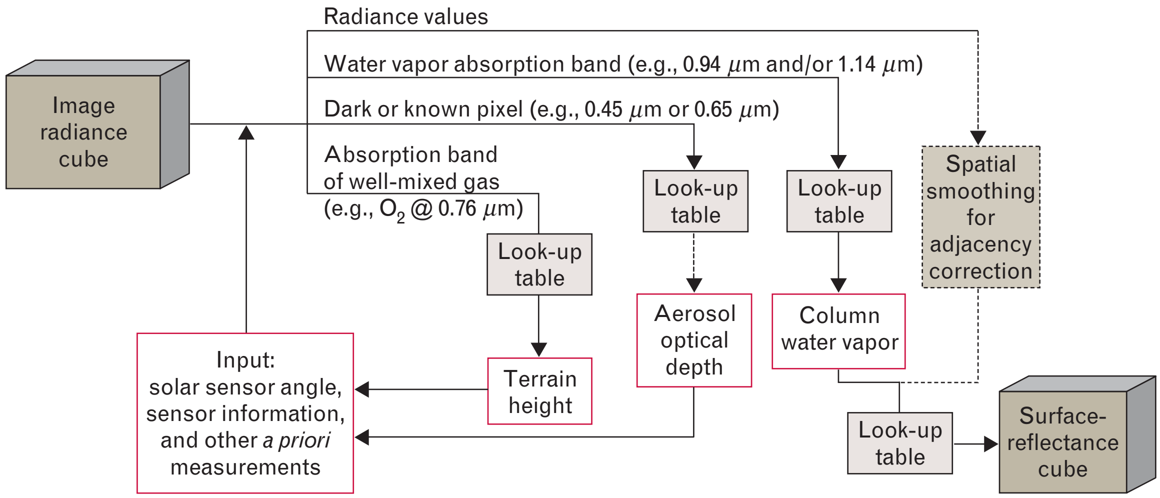

FIGURE 5. Schematic flow of the Fast Line-of-Sight Atmospheric Analysis of Spectral Hypercubes (FLAASH) code. The diagram defines the basic steps used to convert the sensor measured radiance to surface reflectance. Secondary products such as the column water vapor and the aerosol optical depth can also be obtained. The dotted connection lines indicate an optional selection in FLAASH.

count. Because atmospheric concentrations of mixed gases such as O_2, O_3, and CO_2 are generally well known, their absorption properties can be computed quite accurately. The models must treat other gases, for which the concentration is unknown and/or highly variable, such as water vapor, separately. The following section details the approach that both ATREM and FLAASH take to estimate the atmospheric water content of a scene. It was found that the current technique used by ATREM to estimate column water vapor could be improved with the inclusion of a weaker absorption band into the computation. This enhancement to ATREM is discussed below. A comparison of the retrieved surface reflectance from both models for three different scenes follows the water vapor discussion.

Water Vapor Retrieval Methodology

Both ATREM and FLAASH utilize a three-band ratio method to estimate the water vapor transmittance of the intervening atmosphere. The three-band ratio technique selects channels in the 0.94-μm and 1.14-μm water vapor absorption bands [10, 20]. As shown in Figure 6, the water vapor bands are well characterized by the narrowband hyperspectral channels (shown as red horizontal bars in the image). Typically, three to five hyperspectral channels are chosen to represent the strongest portion of the water vapor band. Two more sets of channels located in the off-band window (high transmission) regions, where absorption due to water vapor is small are selected (one set on each side of the water vapor absorption band).

A mean radiance is computed for each of the three channel sets. The two window radiances are combined by using a spectrally weighted average, and a ratio of the water vapor band radiance to the overall window radiance is computed, producing a pseudo-transmittance value. This value is compared with a precomputed table of three-band ratios for the same band specifications over a range of column water vapor amounts, as shown in Figure 7. Ratios are shown for three water vapor bands: the default 0.94-μm and 1.14-μm bands used in both ATREM and FLAASH and the weaker 0.91-μm band. Each band has a distinct array of ratio values, with the 0.91-μm band having the smallest range of ratios for the given span of column water vapor values. Figure 7 shows that the 1.14-μm band provides the greatest sensitivity to water vapor variations for amounts less than 3 cm. For column water vapor amounts greater than about 4 or 5 cm, the ratio values change very little. Thus small variations in the ratio values can lead to large changes in the retrieved column water vapor. Significant errors are possible when dealing with very moist scenes.

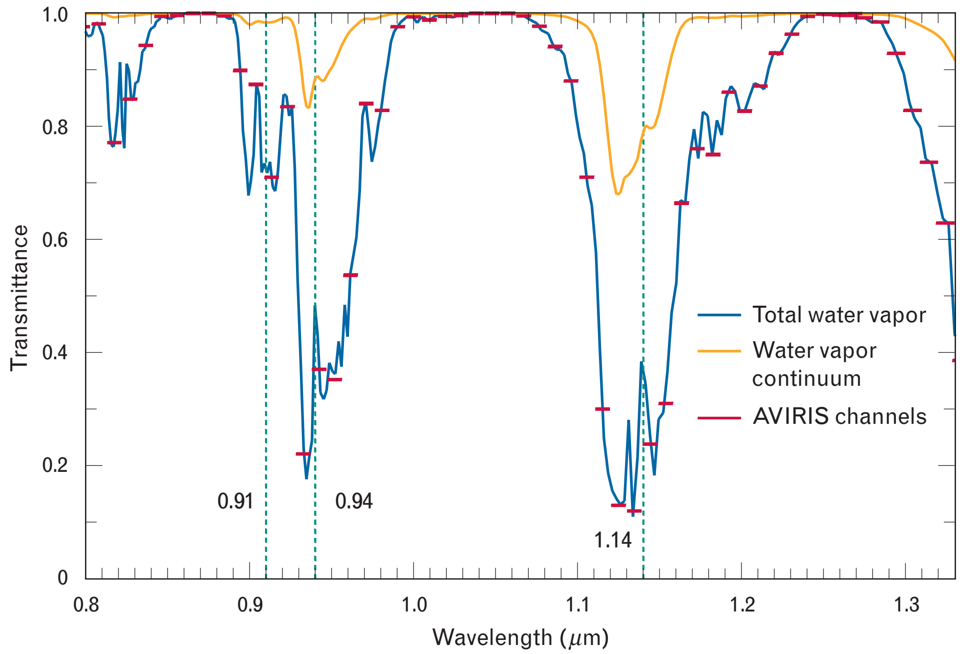

FIGURE 6. Atmospheric transmittance in the region of three water vapor absorption features (lines and continuum) in the near infrared. Nominal Airborne Visible Infrared Imaging Spectrometer (AVIRIS) channels are represented by their 10-nm bandwidths (red horizontal bars positioned near the representative mean channel transmittance).

Water vapor transmittance and column water vapor amounts for ATREM are determined from the closest match to the measured three-band ratio values and are used to define the water vapor characteristics

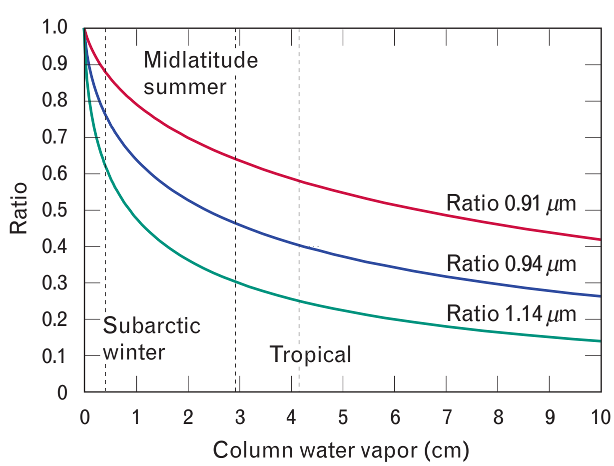

FIGURE 7. Three-band ratios for three water vapor bands in the near-infrared region as a function of the total water vapor content. The ratio value is computed as the water vapor band radiance relative to the adjacent window radiance. Vertical dashed lines represent the column water vapor for three standard atmospheric models.

of the pixel. This procedure is repeated for every pixel in the image. In ATREM, the operation tends to be fast, since it involves a simple ratio calculation and a look-up table (LUT) search for each pixel.

FLAASH uses a slightly different approach to obtain the column water vapor. FLAASH computations depend on separate within-band and window radiances and not the ratio of the two. This process requires a onetime calculation of a two-dimensional LUT and an interpolation step for each pixel. The LUT is generated from MODTRAN calculations of the full gaseous absorption characteristics and aerosol/molecular scattering for each spectral band; therefore, taking the ratio of the two values is not required.

Test Scenes for Water Vapor Retrievals

Hyperspectral data collected from three different locations, summarized in Table 1, were selected for evaluating ATREM and FLAASH retrievals of water vapor. Figure 8 depicts the scenes as false-color images obtained by displaying three channels, one in each of the primary colors (red, green and blue). The channel-color combinations for these figures were chosen

Table 1. Test Scenes for Water Vapor Retrievals from Hyperspectral Data

Hyperspectral Sensor	*Image Location*	*Scene Dimensions (km^2)*	*Date/Time UTC*	*Pixel Resolution (m)*
AVIRIS	Jasper Ridge, California	11 × 10	3 April 1997/2010	20
HYDICE	Keystone (Able), Pennsylvania	0.25 × 0.25	10 April 1997/1730	~2
AVIRIS	Moffett Field, California	11 × 10	20 June 1997/1850	20

to enhance surface feature identification in the displayed images. Different channel combinations can be used to highlight other features such as haze/aerosol clutter and atmospheric moisture content.

Figure 9 displays the derived water vapor images, based on the FLAASH and ATREM retrievals, of column water vapor for the Jasper Ridge case. As shown, the atmosphere was relatively free of water vapor, and results from both algorithms were similar, agreeing well with values derived from nearby National Oceanic and Atmospheric Administration (NOAA)–National Weather Service (NWS) radiosonde observations (0.67 cm of water vapor at 12 UTC, 3 April 1997 and 1.13 cm of water vapor at 00 UTC, 4 April 1997). Similar spatial variability is found in both derived images; the standard deviation is less than 10% of the mean value, which is indicative of a spatially homogeneous water vapor field. Surface features such as roads, a lake, and urban structures are apparent in the ATREM water vapor image and to a lesser extent in the FLAASH image. The appearance of these features is an indication of the failure of the three-band retrieval approach to eliminate the surface-reflectance effect. Retrieval of the column water vapor over water surfaces is a challenging task for atmospheric compensation models because of the extremely low surface radiance signal. Water surfaces are often excluded in the processing for this reason. A key assumption of the retrieval approach is that the surface reflectance varies linearly across the water vapor band such that an average of adjacent window reflectances simulates the value for the absorption band. For some surface features, such as urban areas, this assumption may not be valid. Also, terrain-elevation variations can induce water vapor values to follow the terrain contours. Both ATREM and FLAASH assume a constant elevation across the image; large variations in terrain elevation can result in misleading water vapor features, as can be observed in the left side of the column water vapor images in Figure 9.

In contrast to the Jasper Ridge scene, the Keystone scene represents a moderately moist atmosphere, as shown in Figure 10. The derived water vapor images from ATREM and FLAASH were quite different for this scene. ATREM retrieved unreasonably high water vapor content, while the FLAASH retrieval is close to radiosonde observations and is also climatologically more realistic. One reason for this overestimation of the water vapor may be due to the exclusion of the effects of the water vapor continuum in the ATREM calculations. This possibility is explored more in the next section. Again, for both codes, less than 10% spatial standard deviation was observed across the scene.

The Moffett Field scene, shown in Figure 8, is located approximately 20 km from the Jasper Ridge scene. Both scenes consist primarily of a hilly ridge and an urban area. However, in the FLAASH-derived water vapor image for the Moffett Field scene shown in Figure 11, a moisture gradient can be observed with largest values in the lower left corner, decreasing toward the upper right. The southern portion of the San Francisco Bay is located just to the left (west) of the image. The foothills provide a boundary for the flow of moist air from the bay. This geography is evident both in the image and from the histogram of the water vapor, which clearly shows a bimodal distribution corresponding to the low-lying urban area

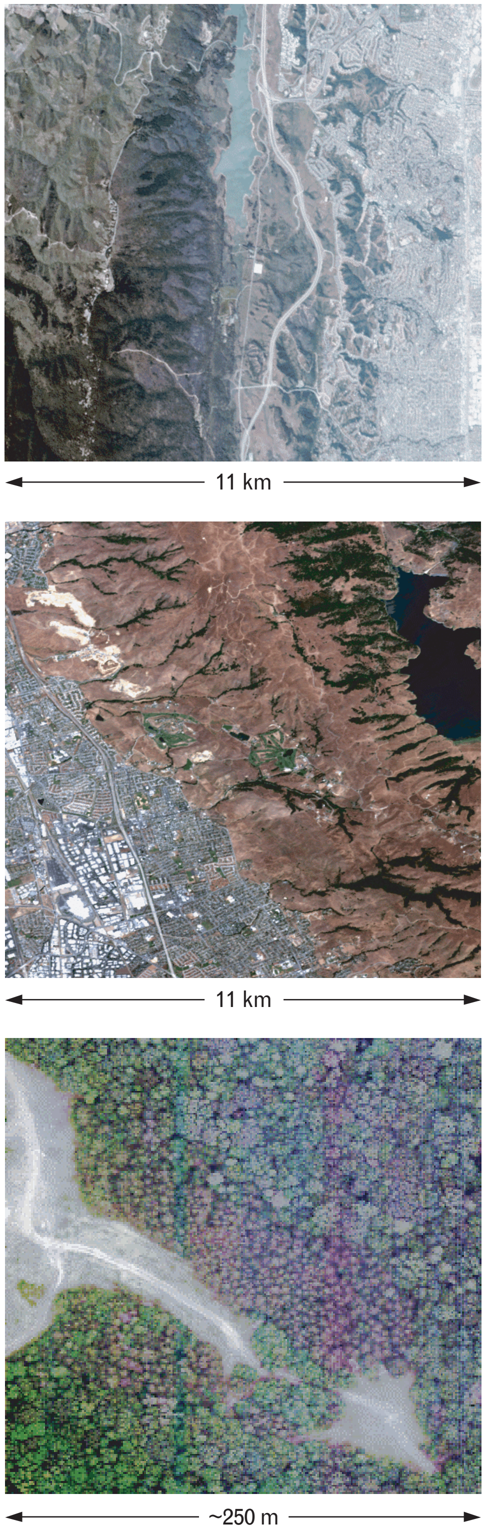

FIGURE 8. AVIRIS and Hyperspectral Digital Imagery Collection Experiment (HYDICE) test images. The top and middle AVIRIS images were collected at Jasper Ridge and near Moffett Field, California, respectively. The bottom HYDICE scene was collected at Keystone, Pennsylvania.

(moist) and the higher-altitude foothills region (dry). Figure 12 displays the retrieved column water vapor amounts for three cross sections in the image. The left side of the abscissa corresponds to the top of the image. The curves in Figure 12 are consistent with the local topography and perceived moisture flow from San Francisco Bay. While the trend from top to bottom of the image along these cross sections is toward increasing water vapor amounts, the fine scale structure displays many features associated with both terrain changes and local water vapor variations.

Enhancements to Water Vapor Retrievals

The apparent overestimation of water vapor by ATREM prompted further analysis. We found that by using channels in the ratio computation offset from the 0.94-μm water vapor band, specifically in the weaker 0.91-μm band, the ATREM ratio calculation produced more reasonable values for moist scenes. ATREM does not include a contribution from the water vapor continuum in its computation of the water vapor effects. From Figure 6, it is clear the continuum provides a significant contribution to the water vapor absorption, which may in part be responsible for the high retrieved column water vapor values. The continuum contribution is negligible at 0.91 μm, so any error due to its omission is minimized. In addition, since the absorption is weaker at 0.91 μm, this band is less sensitive to higher amounts of moisture. When we used the 0.91-μm band ratio, the mean water vapor amounts that ATREM computed for the Keystone case reduced from 6.14 to 5.49 cm, a modest reduction in the right direction, but still well above the observed value.

To investigate further the use of the 0.91-μm band ratio, we generated simulated AVIRIS data from MODTRAN calculations for clear-sky, uniform surface-reflectance scenes under various moisture and rural aerosol conditions. As shown in Table 2, retrievals of the column water vapor amounts from ATREM for the simulated data with the 0.91-μm band were close ($\Delta < 0.5$ cm) to the input model values for these simulated test cases and to those obtained by FLAASH. The near-perfect retrieval of water vapor by FLAASH is somewhat misleading in that both the simulated AVIRIS data and the FLAASH model are

Table 2. Retrieved Water Vapor for Simulated AVIRIS Test Cases*

Model Atmosphere	*Surface Albedo*	*Visual Range (km)*	*Water Column (cm)*	*Derived Column Water Vapor (cm)* ATREM			FLAASH	
Wavelength**				0.91 μm	0.94 μm	1.14 μm	0.94 μm	1.14 μm
Subarctic winter	0.2	23	0.42	0.42	0.47	0.39	0.42	0.41
Subarctic winter	0.4	23	0.42	0.43	0.48	0.40	0.42	0.42
Midlatitude summer	0.2	10	2.93	2.98	3.79	4.00	2.92	2.94
Midlatitude summer	0.4	10	2.93	3.12	4.01	4.21	2.92	2.92
Tropical	0.2	5	4.11	4.40	5.60	6.10	4.11	4.19
Tropical	0.4	5	4.11	4.66	6.04	6.52	4.11	4.16

* All cases were generated by using MODTRAN with a rural aerosol model and a 30° solar zenith angle.
** These wavelengths correspond to the water vapor band-ratio curves shown in Figure 7.

dependent on MODTRAN computations. It is therefore not unexpected that the FLAASH results were accurate under these circumstances.

Surface-Reflectance Comparison

In this section, we compare the model retrieved surface reflectance for the three test scenes listed in Table 1. For these three scenes, depicted in Figure 8, sets of three to four pixels were chosen whose location matched specific surface features. For the Jasper Ridge AVIRIS image, pixels representing the radiance from a paved road, an urban area, ridgeline vegetation, and a lake were examined and the spectral surface reflectances were retrieved by using both FLAASH and ATREM atmospheric compensation models. Identical input parameter specifications de-

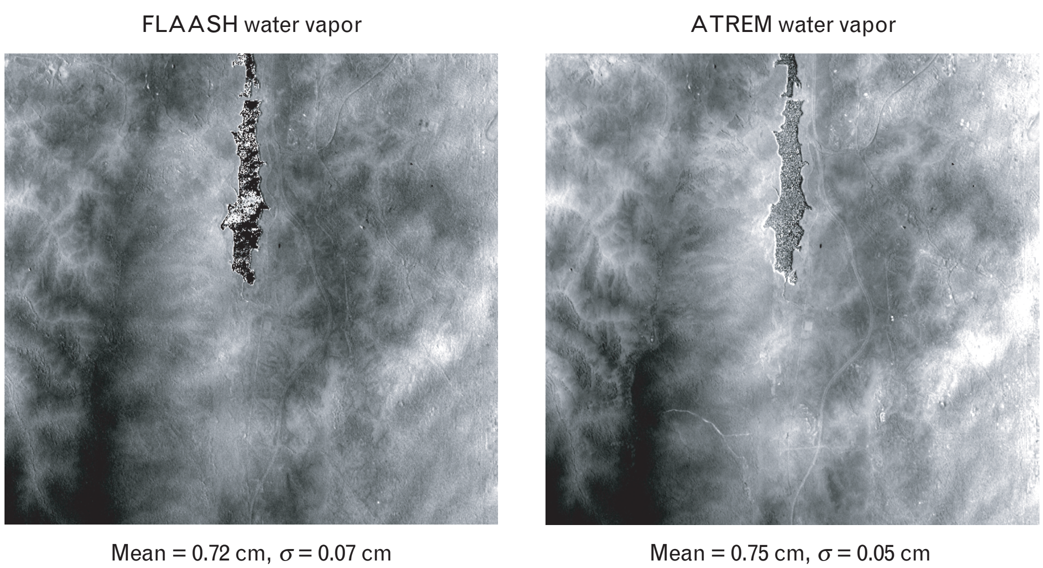

FIGURE 9. FLAASH-computed and ATREM-computed column water vapor images for the AVIRIS Jasper Ridge Test Scene (2010 UTC on 3 April 1997). Mean and standard-deviation column water vapor values are shown for both models. Surface features such as roads, a lake, and urban structures are apparent in the ATREM water vapor image and to a lesser extent in the FLAASH image.

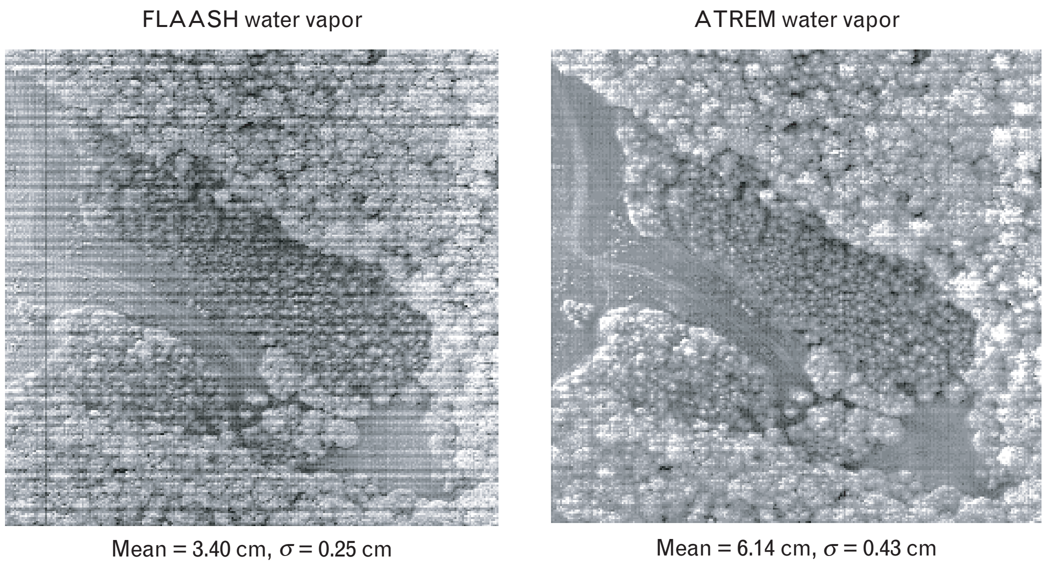

FIGURE 10. FLAASH-computed and ATREM-computed water vapor images for the HYDICE Keystone Test Scene (1730 UTC on 10 April 1997). Mean and standard-deviation column water vapor values are shown for both models; nearby radiosonde values of 2.97 and 3.25 cm were observed.

scribing the ambient scene characteristics were provided to both models. The Jasper Ridge image was collected on a clear, dry day at 2010 UTC (1210 PST). Figure 13 shows the resulting retrieved surface-reflectance comparison. The models compare well, especially for the water pixel and the vegetation pixel (outside the near-infrared water vapor absorption region). Both the road and urban comparisons show slightly higher retrieved reflectance differences (still less than 0.02), most noticeably near the weak water vapor absorption bands and the 1.6-μm atmospheric window. In Figure 13 and subsequent figures, the re-

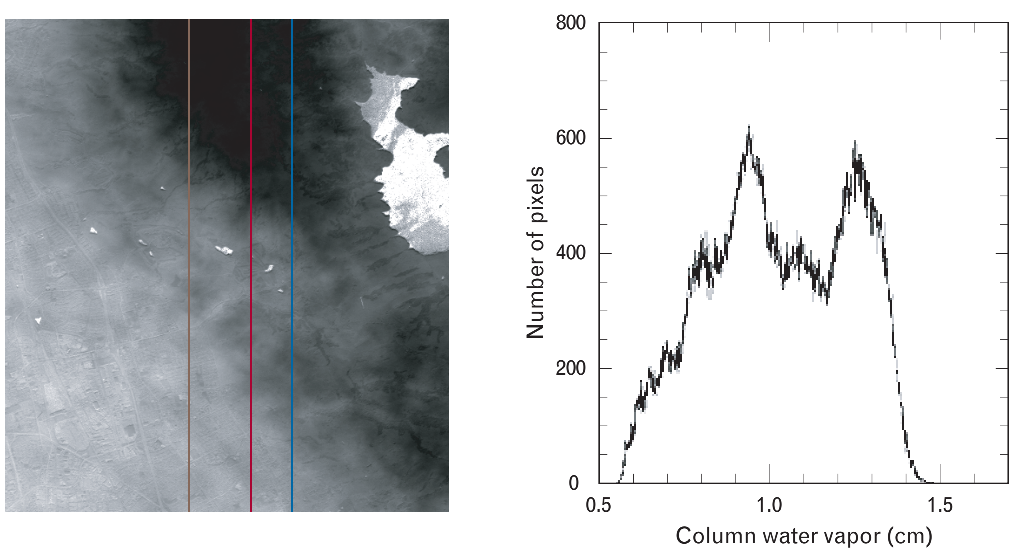

FIGURE 11. Retrieved integrated water vapor AVIRIS image from the Moffett Field test case (1850 UTC on 20 June 1997) and the associated histogram showing a bimodal distribution of water vapor in the image. Vertical lines correspond to column water vapor cross sections shown in Figure 12.

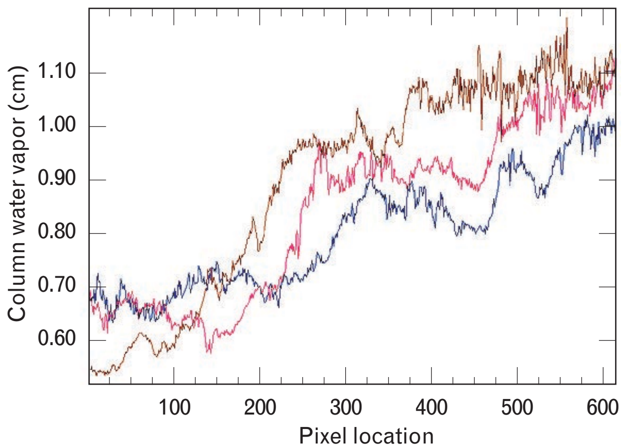

FIGURE 12. FLAASH-computed column water vapor amount (cm), shown as a function of pixel location along cross sections from top to bottom of the AVIRIS image in Figure 11. The three curves correspond by color to the cross-section lines in that image.

trieved surface reflectance is zeroed out near the 1.38- and 1.88-μm water vapor absorption bands, since the component of the measured signal emanating from the surface is almost completely masked by the strong water vapor absorption.

In the Keystone HYDICE image, the four pixels chosen represented the radiance from a bare soil surface, an unpaved road, and two different types of trees. The Keystone data were collected in August during a typical warm, hazy day. Identical input parameters were again provided to the models. Figure 14 shows the spectral surface reflectances retrieved by using ATREM and FLAASH. The comparison is good, especially above 1.5 μm. The largest differences occur near the water vapor bands where exaggerations of reflectance values, or spiking, occurs. Spiking may be due to inaccurate band wavelength assignment. The spiking artifact is largest for ATREM retrievals, presumably because of its difficulty in processing scenes where moist atmospheric conditions prevail. Inaccurate spectral wavelength values tend to enhance the moisture retrieval errors. FLAASH also displays some reflectance spiking, but to a lesser degree than ATREM.

Data for the third test scene were collected near Moffett Field, California. Ambient conditions observed at the time of the collection were somewhat warmer and more humid than the Jasper Ridge scene (located approximately 20 km to the northwest), but still much dryer than the HYDICE scene discussed previously. Figure 15 shows the retrieved surface reflectances modeled by ATREM and FLAASH for three surface features (paved road, green ridge, and

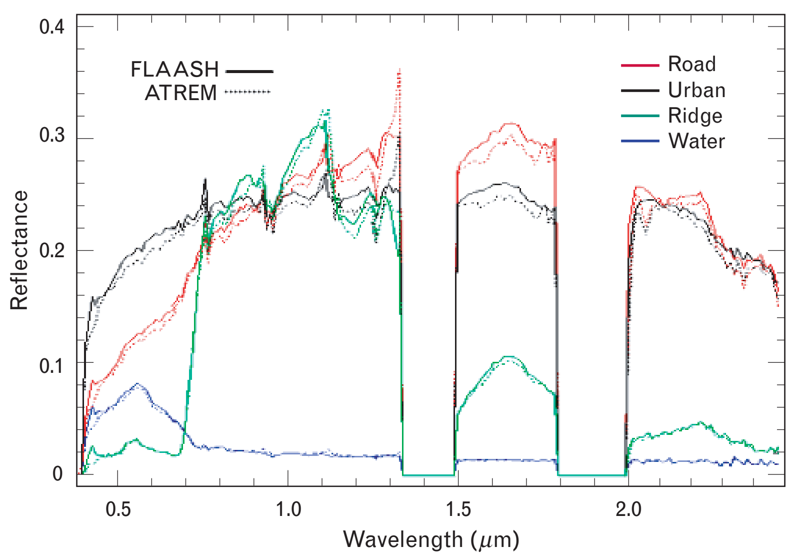

FIGURE 13. Comparison of retrieved surface reflectances from ATREM and FLAASH for the Jasper Ridge AVIRIS image. Four surface types—road, urban, ridge, and water—were located in the image and their spectral surface reflectances retrieved.

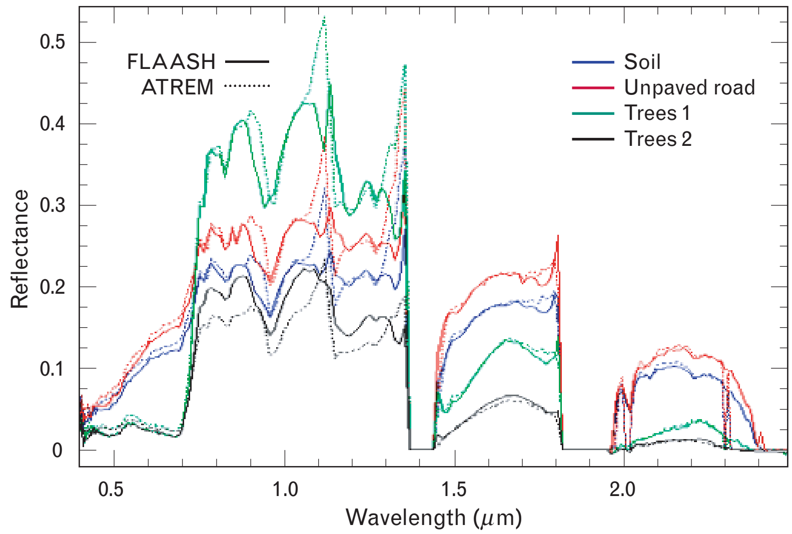

FIGURE 14. Comparison of retrieved surface reflectances from ATREM and FLAASH for the Keystone HYDICE image. Four surface types—soil, unpaved road, and two types of trees—were located in the image and their spectral surface reflectances retrieved.

brown grass). The ATREM and FLAASH results compare well, with absolute model differences in retrieved reflectance of less than 0.01 across the spectrum for all three surface features. Interestingly, the reflection spikes seen in the other two comparisons are less prominent here; the reason is not apparent.

For all three cases, the comparison between ATREM and FLAASH was quite good. The largest differences were observed in the 0.6-to-1.1-μm spectral region, where numerous water vapor absorption bands can cause the retrieved surface reflectance to exhibit sharp spikes with differences greater than 0.05

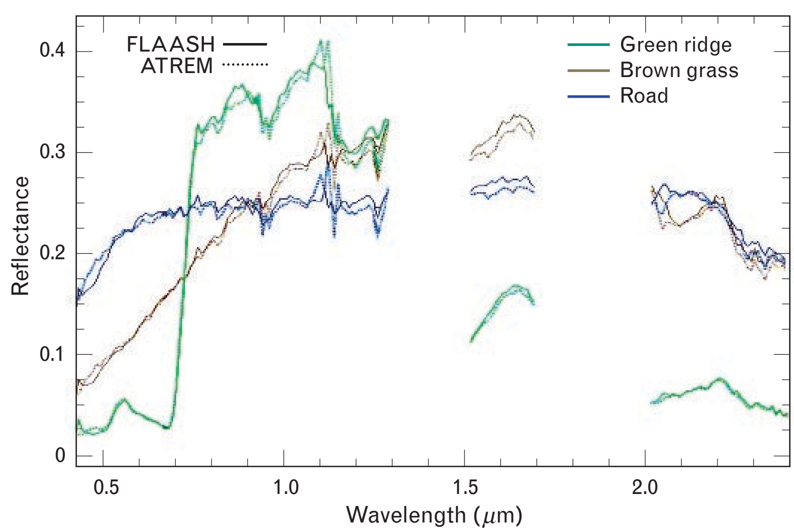

FIGURE 15. Comparison of retrieved surface reflectances from ATREM and FLAASH for the Moffett Field AVIRIS image. Three surface types—green ridge, brown grass, and paved road—were located in the image and their spectral surface reflectances retrieved.

from the accepted truth value. There was also a small increase in the model differences for the moist, humid HYDICE case over the drier AVIRIS cases. This difference was not believed to be an instrument artifact, but rather a known difficulty with ATREM in determining the column water vapor for vapor-laden scenes and the subsequent effects on retrieval computations.

Sensitivity to Input Parameter Specification

As discussed previously, atmospheric compensation models have been developed to isolate the surface reflectance signal and remove unwanted atmospheric and illumination affects. These models all require some *a priori* information about the atmospheric and surface characteristics, which is used in the compensation process. Incomplete knowledge or inaccurate estimation of certain input parameters adds a degree of error to the retrieval of the surface reflectance. To illustrate the sensitivity of the retrieved surface reflectance ρ_s to mis-specification of FLAASH input parameters, we performed a study by using estimated input parameters to depict the atmospheric state for the Moffett Field AVIRIS image shown in Figure 8. The study compared retrieved surface reflectance at three specific locations in the image obtained from FLAASH runs by using two sets of physically reasonable input specifications. These results, along with the input specifications for both runs, are given in Figure 16. Under these circumstances, differences in the retrieved ρ_s values can range up to 0.11 (absolute difference), depending on the surface feature and the wavelength. For most remote sensing applications, these errors are unacceptable. Accurate specification of the input parameters is clearly an important part of the hyperspectral image analysis process.

Further sensitivity analysis utilized simulated AVIRIS data generated by using MODTRAN calculations for clear-sky, uniform surface reflectance scenes under three different moisture and visibility conditions. The conditions ranged from a relatively clear and dry atmosphere to one with hazy, wet conditions, as listed earlier in Table 2. Using these test-data cubes, we can vary specific input parameters to the atmospheric compensation models and determine the effect they have on the retrieved surface reflectance.

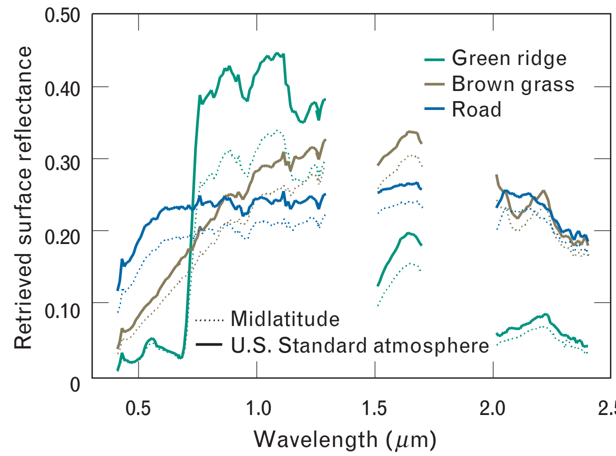

FIGURE 16. Sensitivity of FLAASH to atmospheric characterization for surface features. The spectral surface reflectances are retrieved for three surface types in the AVIRIS Moffett Field scene by using two different sets of model-input conditions. The input specifications for the two runs are (1) midlatitude summer atmosphere, urban aerosol model, and 16-km visibility, and (2) U.S. Standard atmosphere, rural aerosol model, 60-km visibility, and time offset error of 20 minutes (equivalent to a 2° error in the solar zenith angle).

Comparison to the known ρ_s provides an absolute measure of the sensitivity to the varied input parameter. The following subsections attempt to isolate the degree to which errors in each of the following atmospheric compensation model-input parameters can affect the final retrieved ρ_s: visibility, aerosol model, atmospheric model, and solar zenith angle.

Visibility

Atmospheric visibility is inversely proportional to the optical depth. The optical depth varies in part as a function of the aerosol and moisture content of the lower 2 to 3 km of the atmosphere. Water vapor absorbs and aerosols scatter the radiance in proportion to their concentration. In general, the higher the aerosol concentration (or optical depth), the lower the visibility. Hence visibility is an indicator of the amount of attenuation in the lower atmosphere and therefore a useful characterization for the atmospheric compensation process.

To examine the sensitivity of the models (FLAASH and ATREM) to uncertainty in visibility, we used two model surface-reflectance values—0.2 and 0.4—both spectrally invariant. Figure 17 displays the absolute difference in the surface reflectance (shown as the retrieved reflectivity error) for FLAASH runs using three assumed input visibilities (5, 10, and 23 km) at the two model ρ_s values. The error is computed by subtracting the model ρ_s values (0.2 and 0.4) from the retrieved ρ_s values, for three FLAASH runs with the three different visibility values. All runs utilized a midlatitude summer atmosphere with a rural aerosol model. The "truth" visibility value is 10 km. Because MODTRAN and FLAASH share the same radiative-transfer code, we expect FLAASH will accurately retrieve the test cube reflectances, given the correct input parameters. Such is the case, as denoted by the green line in Figure 17.

The reflectivity errors for both the 5-km and 23-km visibility runs are within ± 0.03 of the true values except near the 0.94-μm and 1.14-μm water vapor absorption bands. The sloping error lines in the shortwave region are the result of the increased effect of aerosol and Rayleigh scattering. At these wavelengths, the reflectance due to aerosol and Rayleigh scattering dominates the measured reflectance signal (for lower ρ_s values, 0.2). When the visibility of a scene is underspecified (hazier), the resulting increase in perceived atmospheric reflectance is compensated for by an underestimation of ρ_s. In the near infrared, where atmospheric scattering is not as dominant, the perceived reduction in the atmospheric transmission is compensated for by an overestimation of the surface reflectance. An analogous situation results for an overspecification of the visibility (clearer), although the error values are not quite as large.

Figure 18 shows the retrieved reflectance errors for the ATREM runs. ATREM does not reproduce the surface-reflectance values as accurately as FLAASH for a number of reasons. ATREM model parameterizations are based on less accurate molecular band models and different aerosol models than those used in MODTRAN. Also, ATREM decouples the absorption from the scattering processes in the radiative-transfer model calculations. This effect can be seen in Figure 18(a), in which the model truth ρ_s values are, as before, subtracted from the retrieved ρ_s values for the three optimal visibility values (5, 10, and 23 km). Here the water vapor absorption line structure is still quite apparent in the spectral reflectance curves. To remove the absorption and other model effects from the reflectance, we subtract the ATREM-retrieved ρ_s values for the 10-km visibility run (the truth visibility) from the retrieved ρ_s values for the other visibility runs, with results shown in Figure 18(b). These error curves, which are in effect compensated for model-induced differences, are much more similar to what FLAASH produces.

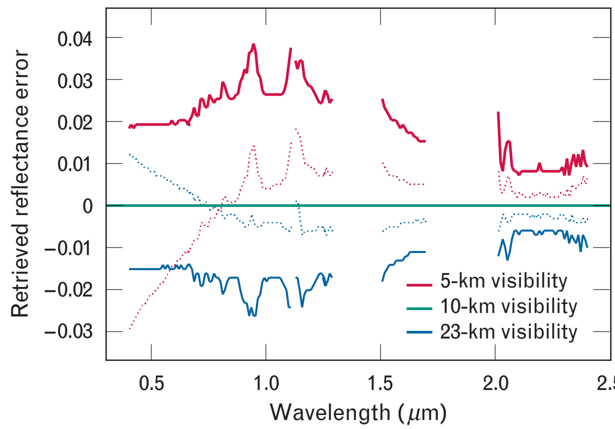

FIGURE 17. FLAASH-retrieved surface reflectance minus model-input surface reflectance for three input visibility conditions. The model-input surface-reflectance values are either 0.2 (dotted curves) or 0.4 (solid curves) and are spectrally invariant. The true scene visibility is 10 km.

For surfaces with moderate or high reflectances, if the value assumed for the visibility, as input to the model, is greater (clearer) than the actual "truth" visibility of the scene, the retrieved surface reflectance is underestimated. The converse is also true: an input visibility smaller (more opaque) than the "truth" visibility results in an overestimate of the surface-reflectance values.

Aerosol-Model Type

There are a variety of predefined aerosol models that are available for use in ATREM and FLAASH. The models typically represent the characteristics of aerosols found in the lowest 2 km (within the atmospheric boundary layer) for a set of basic topographic types: desert, maritime, rural, and urban. Each model consists of a weighted mixture of four basic kinds of aerosol particles: dust, oceanic, water-soluble, and soot. Urban, for example, has more soot and water-soluble

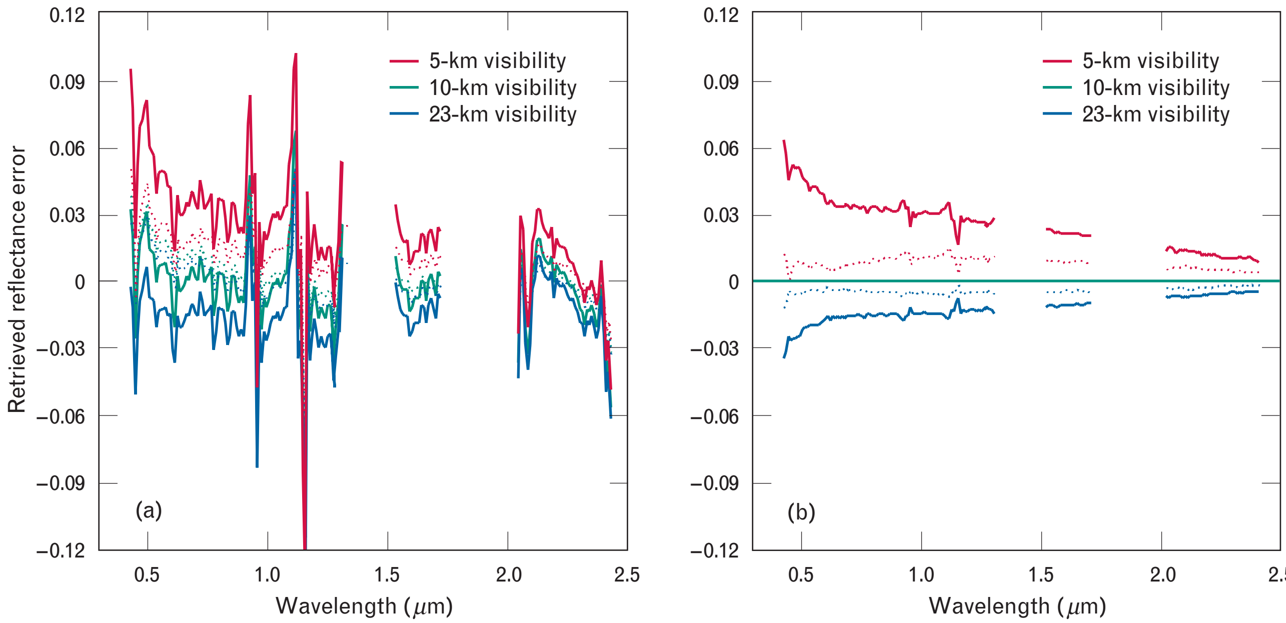

FIGURE 18. ATREM-retrieved reflectances with (a) model-input surface reflectance subtracted and (b) the ATREM retrieved reflectance using the true visibility as input subtracted, for three input visibilities. Truth scene values are midlatitude summer atmosphere with a rural aerosol model and 10-km visibility. The model-input surface-reflectance values are either 0.2 (dotted curves) or 0.4 (solid curves) and are spectrally invariant.

particles than maritime, which consists of predominantly oceanic particles such as salt and sea-foam evaporates. The rural (or continental) aerosol model consists of a large percentage of dust particles. With such a diversity of scatterers, the choice of an aerosol model for a particular scene can have a significant effect on the radiative transfer in the lower atmosphere and on the retrieved surface reflectance.

Figure 19 displays the sensitivity of the FLAASH-retrieved reflectance to various aerosol models for two highly different atmospheres. For the dry and relatively clear rural aerosol case in Figure 19(a), the effect of varying the aerosol model produces errors in retrieved reflectance of less than ± 0.02, except at visible wavelengths, where the effect gradually increases with decreasing wavelength for the urban model only. The results obtained with the urban aerosol model seem to be most sensitive to the atmospheric composition, as can be seen for the tropical, hazy test case in Figure 19(b). While the other model errors in retrieved reflectance are generally less than 0.04, the errors for the urban model results are within 0.10 at wavelengths greater than 1 μm but increase rapidly at shorter wavelengths. This behavior seems to indicate a strong sensitivity of the urban model results to moisture and visibility. The significant degree of soot in the model can have a strong absorbing effect under low visibility (high aerosol density) conditions masking the signal from the surface and producing erroneous results from the model.

Atmospheric Model

In MODTRAN, there are six choices for model atmospheres. Each model atmosphere includes a set of profiles defining the pressure, temperature, air density, water vapor, and ozone characteristics representative of the seasonal conditions for a geographic region. Surface temperatures for these atmospheres vary from 257 K for a subarctic wintertime atmosphere to 300 K for a tropical atmosphere. Table 2 shows that the amount of moisture an atmosphere can support varies greatly over the range of standard atmospheres used in MODTRAN. This variation is a function of the temperature profile: i.e., colder temperatures saturate at lower levels of moisture than higher temperatures, which limits the choices of model atmospheres for a specific scene. Errors result if a model atmosphere incapable of supporting the moisture

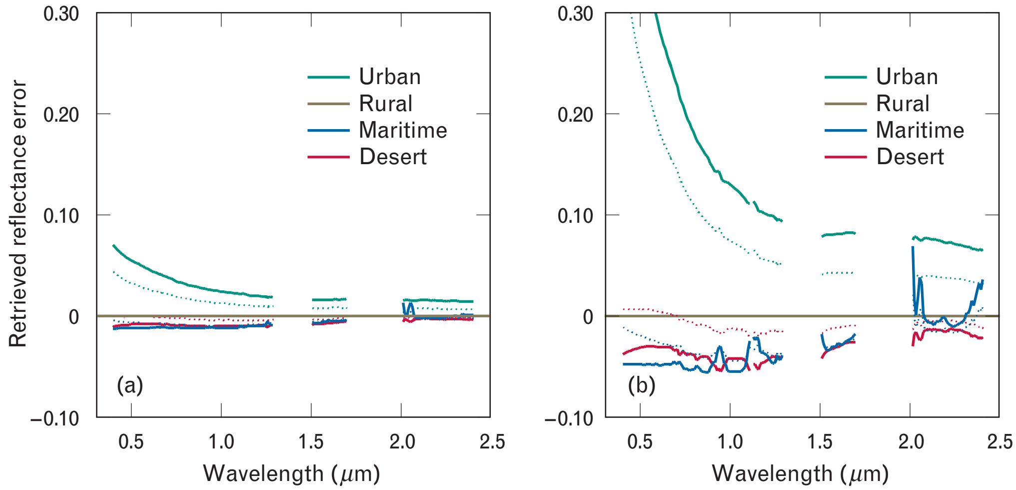

FIGURE 19. FLAASH-retrieved reflectance errors for four aerosol model types. Values are shown for two atmospheric scenes, (a) dry and relatively clear (subarctic winter atmosphere, rural aerosol model, 23-km visibility) and (b) humid and hazy (tropical atmosphere, rural aerosol model, and 5-km visibility). The model-input surface-reflectance values are either 0.2 (dotted curves) or 0.4 (solid curves) and are spectrally invariant.

content of the scene is used. A set of model atmospheres was used with this limitation in mind as input to FLAASH to study the sensitivity of the model retrievals to changes in the atmospheric profiles.

Results of varying the atmospheric model type (and associated moisture and temperature profile) seem to have little effect on the retrieved reflectance values as long as the input model temperature profile can support the total column water vapor of the scene. In Figure 20, retrieved reflectance errors are generally less than ± 0.01, except near the water vapor absorption bands. FLAASH performs well in estimating the actual water vapor content when using any moderately moist atmospheric profile. Similarly, in relatively dry scenes, FLAASH internally adjusts the moisture content of the model to provide the closest approximation to the scene moisture amount. However, the converse does not always apply. Using a cold, dry atmospheric model as input when processing a moist scene can lead to erroneous results.

Solar Zenith Angle

For a typical AVIRIS scene, the date, time, and location are known accurately; therefore, the solar zenith angle can be computed with high precision. The plots in Figure 21 show the errors incurred by using a constant solar zenith angle (SZA) assumption for all scenes taken at different times during a flight. For a forty-minute flight centered in time at solar noon, the SZA varies by approximately 2° (from a mid-flight value of 30°) and the retrieved reflectance errors are within ± 0.04. As would be expected, these errors increase for a two-hour flight exceeding 0.10 at visible wavelengths. Specifying input of a larger SZA than the true value results in an overestimate of the retrieved reflectance value; the converse is also true. It is

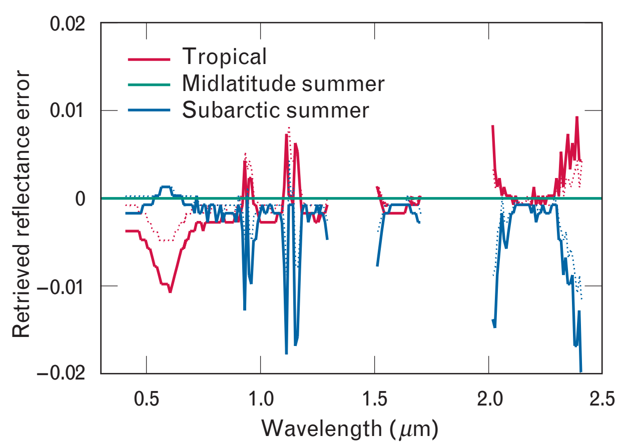

FIGURE 20. FLAASH-retrieved reflectance errors for runs made with three atmospheric models (truth atmosphere is midlatitude summer). The model-input surface-reflectance values are either 0.2 (dotted curves) or 0.4 (solid curves) and are spectrally invariant.

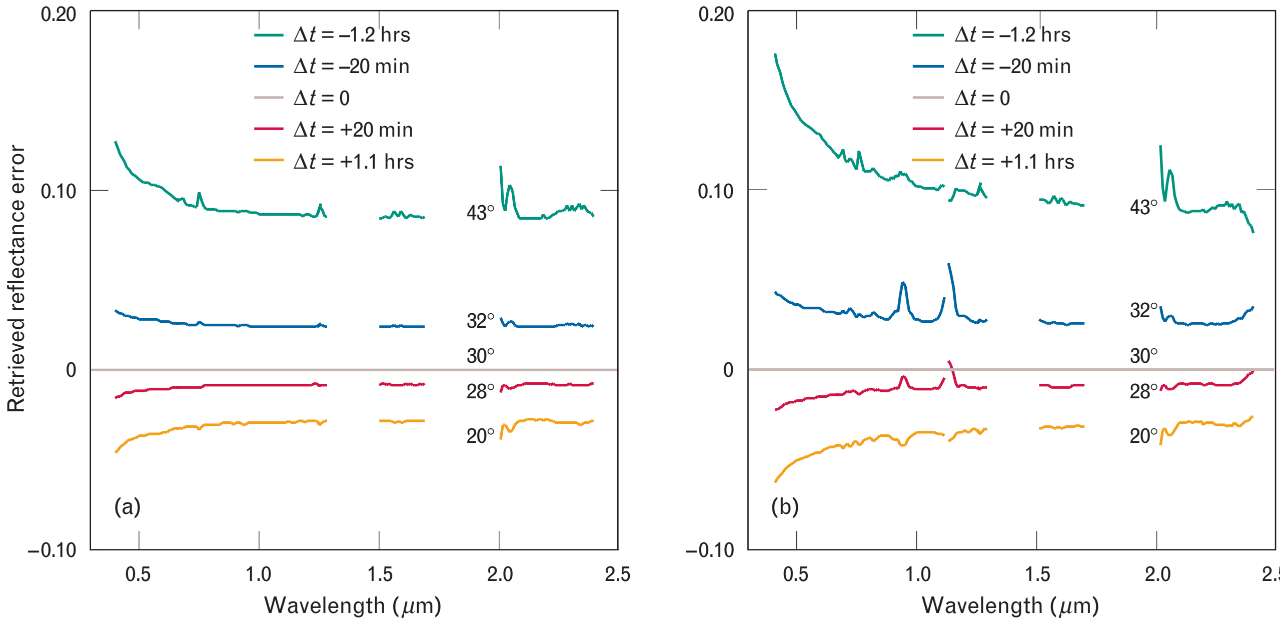

FIGURE 21. FLAASH-retrieved reflectance errors for a constant solar zenith angle (SZA) in the model calculations for two flight lengths (40 minutes and ~2 hours). Values are shown for two atmospheric scenes, (a) dry and relatively clear (subarctic winter atmosphere, rural aerosol model, 23-km visibility) and (b) humid and hazy (tropical atmosphere, rural aerosol model and 5-km visibility), both with a true SZA value of 30°. The SZA for each of the offset times is shown in the graphs.

also useful to note that errors tend to be smaller at low SZAs (high sun elevation) than for high SZAs (low sun elevation) because of the differing rates of change in the SZA at those times.

Computational Complexity

Until now, this discussion on the merits of the atmospheric compensation models has not considered the effect these operations have on the overall computational budget for processing hyperspectral data cubes. The decision on how best to use these models requires an inquiry into the benefits versus computational costs. The primary metric for computation time/complexity is the number of floating-point operations (FLOPs) per data processing task. The FLOPs metric has the advantage of being independent of the processor speed. On the other hand, it does not take into account the cost of I/O (file reading and writing) time, which can be a significant portion of the atmospheric compensation processing time.

Basic Atmospheric Compensation Computational Costs

ATREM calculates the reflectance for each pixel analytically from Equation 2. The solution to this equation requires 6 FLOPs and 3 one-dimensional LUTs (each comprising 3 FLOPs), for a total expected number of FLOPs per pixel per channel of 15. For the FLAASH model, the computational complexity is directly related to the selected complexity of the model analysis. With the adjacency option turned off, FLAASH's calculation is mathematically equivalent to ATREM's, so it is possible to use equivalent code and achieve the same number of FLOPs (15 per pixel per channel). With the adjacency option activated, the number of FLOPs per pixel per channel is expected to increase by a factor of two or three. [21]. An alternative method that involves tabulating parameters from Equation 1 in multidimensional LUTs can result in a computational savings of one-third, yielding a value similar to that for the ATREM model.

Computational Costs of Enhanced Atmospheric Compensation

While ATREM is limited to the basic atmospheric compensation process described above, a number of enhancements to the basic FLAASH processing can have a considerable impact on the net computational burden. These enhancements include compensation for nonuniform aerosol content, sensor angular field-of-view variations, cirrus clouds, spectral polishing, and channel wavelength variations. While each enhancement can provide improved surface-reflectance retrievals under certain scenarios, they all require further processing of the data.

After clouds and water vapor, aerosol amount (as indicated by the visibility parameter) is the next most variable constituent in the atmosphere. FLAASH utilizes an approach that finds dark (low reflectance) pixels in an image and performs an extended radiative transfer calculation to obtain a number of visibility values for the scene [22]. While the computational requirements increase in proportion to the number of visibility values determined, a doubling of the number of FLOPs is not an unrealistic estimate.

Across a scene, the line of sight (LOS) to the sensor varies. For near-nadir views, most atmospheric compensation codes assume a single LOS associated with the center of a scene. However, for off-nadir measurements, it may be necessary to perform the radiative-transfer calculations at multiple viewing angles to account for the variations in absorber column densities. The increased FLOPs required to account for this added computational burden are similar to the aerosol content computation.

The ability to identify thin cirrus clouds has been demonstrated by using spectral channels located in water vapor bands, and the potential exists for compensating the surface reflectance to account for the presence of clouds. One method involves the subtraction of a cloud radiance or reflectance signal from the observed radiance [11]. An approximate reflectance or radiance post-processing method requires only a few additional FLOPs per pixel channel. A similar method is being implemented in FLAASH [23].

Spectral *polishing* is a mathematical method for removing artifacts from reflectance spectra. When properly implemented, it dramatically reduces spurious, systematic spectral structure due to wavelength registration errors and molecular absorption residuals while leaving true spectral features intact. A number of processing steps are involved, including spectral smoothing, reference-pixel selection, scaling parameter determination, and application of the linear transformation to the data cube. Since polishing is a post-processing step, the computation time simply adds to that required to generate the original reflectance spectra, an increase of 6 to 12 FLOPs per pixel per channel.

Spectral *smile* refers to a wavelength calibration problem such as that experienced with the HYDICE spectrograph sensor. The problem arises from the tendency of spectrographs to have a slight variation in dispersion along the dimension of the entrance slit. This means that each row of the array has a slightly different wavelength calibration, which translates into small, known spectral shifts in the data that depend on the pixel location or sample number along the cross-track direction of the data cube. One method of compensating for smile is through spectral polishing. Another method is to compensate explicitly for the wavelength shifts in the atmospheric compensation algorithm. The latter can result in an increase in FLOPs analogous to the aerosol visibility determination.

Table 3 shows a summary of the increase in computational burden due to the enhancements to the FLAASH code. We see that correcting for aerosol or LOS angle variations can significantly increase the computational burden. Other enhancements such as spectral polishing and smile compensation are relatively efficient and provide little additional computation.

Table 3. Increase in Computational Burden Associated with FLAASH Code Enhancements

FLAASH Enhancement	*FLOPs per pixel per channel*
Aerosol compensation	Double
Sensor angular field-of-view correction	Double
Thin cloud (cirrus) compensation	Add 5–10
Spectral polishing	Add 6–25
Smile correction	Add 0–32

FLOPs Measurements

The computationally significant components for atmospheric compensation include the radiative-transfer calculations to set up the basic reflectance retrieval, perform the basic retrieval, and make any additional computations needed to enhance the basic retrieval. Below we break down each of these components into computational tasks to determine the total computational burden.

Radiative-transfer calculations for ATREM runs were obtained by computing the number of FLOPs for scenes with various pixel dimensions and extrapolating the curve (assuming a linear change in FLOPs with number of pixels) to the limit as the number of pixels approaches zero. This value depicts the computational burden of the radiative-transfer calculations and was found to be 8×10^8. While FLAASH has a number of variations regarding how the radiative-transfer calculations are obtained, for a typical model run, the computed FLOPs count was 7×10^{10}, approximately two orders of magnitude greater than the ATREM run.

The total FLOPs may be approximated as the sum of the radiative-transfer FLOPs and the reflectance-retrieval FLOPs, of which the latter scales with the number of pixels and channels. Estimated results for a 200-channel sensor are shown in Figure 22 as a function of the number of pixels for the current FLAASH and ATREM codes, for an optimized FLAASH, and for an optimized version of FLAASH's adjacency-corrected method. Figure 22 shows that the performance of optimized versions of FLAASH is similar in computational burden to ATREM.

Implications and Alternatives

Compensating for the atmospheric effects for a full frame of hyperspectral data can mean processing millions of pixels of spectral information, a time-consuming task. Various methods have been explored to reduce the amount of compensation needed to analyze a scene. Anomaly identification is a method that involves identifying small numbers of pixels that are spectrally unique. These unique groups of pixels take up only a very small portion of the image. The technique can be applied to data prior to correcting for atmospheric effects. Typically, anomaly identification is used as an initial filtering step to select a small subset of potentially significant pixels from the scene. The atmospheric compensation can be applied to that subset of pixels rather than to the entire data cube, saving computation time.

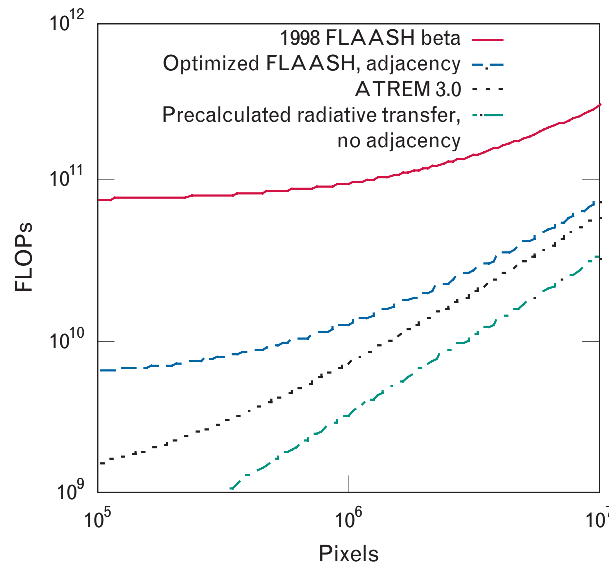

FIGURE 22. Estimated floating-point operations (FLOPs) versus data-cube size for selected atmospheric compensation methods.

With FLAASH, there are several possibilities for speeding up the calculations. Using a coarser band model (15 cm^{-1} versus 1 cm^{-1}) can reduce the FLOPs for a typical run by an order of magnitude. Coarser atmospheric layering can save an additional factor of two. Another approach is to eliminate the radiative-transfer calculation step completely by interpolating from a comprehensive precalculated database that covers all anticipated geometries and atmospheric conditions.

Water vapor computations are normally performed on a pixel-by-pixel basis. Some computation time can be saved if this operation is performed on a regional scale. For example, a clustering type of algorithm could be applied to the scene radiance (or on the measured three-band radiance ratios) to group pixels with similar water vapor characteristics and to reduce the amount of processing time required.

Currently, physics-based and pixel-level atmospheric compensation algorithms are computationally burdensome. Achieving efficient atmospheric compensation may require the use of a multiprocessor computing system. Many aspects of the atmospheric compensation process can be applied simultaneously to individual pixels by dividing the workload among the processors, which could speed up the execution time by an order of magnitude or more.

Summary

In this article, hyperspectral measurements in the visible, near-infrared, and shortwave-infrared reflected spectrum collected by the AVIRIS and HYDICE airborne sensors have been used to compare retrieved values of column water vapor and surface reflectance obtained from the ATREM and FLAASH atmospheric compensation models. ATREM and FLAASH, two commonly used physics-based atmospheric compensation models, were also evaluated for sensitivity to the specification of scene characterization input parameters and respective computational complexity.

Both models retrieved similar column water vapor fields for two relatively dry scenes while a notable difference was observed for a scene collected during a warm and humid day. The mean ATREM-retrieved column water vapor for this warm humid scene was significantly larger than those observed by a nearby radiosonde. The exclusion of the effects of the water vapor continuum in the ATREM model calculations is believed to contribute in part to this error, which was confirmed by the improved results from using the weaker 0.91-μm water vapor band in the water vapor calculations. However, the approach used by ATREM for column water vapor estimation displays limited sensitivity for column water vapor values over 3 cm (small variations in the computed band ratio result in large changes in the estimated column water vapor), which would also contribute to the overestimation. The effect of the inaccurate water vapor estimation was most notable in the retrieved surface reflectance for the near infrared region, where spectral variations in water vapor absorption are common.

To retrieve the surface reflectance, both ATREM and FLAASH require some knowledge of the scene characteristics, which in general are not precisely known and must be estimated from available scene information. We assessed the sensitivity to incomplete knowledge or inaccurate estimation of specific input parameters in terms of the degree of error to the retrieval of the surface reflectance. Results of our study show that certain variations in the inputs to the atmospheric compensation models produce retrieved reflectance differences near 0.1; these errors can be cumulative as we showed in one example. Collection of ambient atmospheric and surface information during hyperspectral data acquisition is the best strategy for avoiding this type of processing error.

An examination of the computational budget for processing hyperspectral data cubes showed that optimized versions of the more complex FLAASH model are similar in computational costs to those of ATREM model. However, enhancements to the FLAASH processing, including computations with nonuniform aerosol content, sensor angular LOS variations, spectral polishing, and channel wavelength corrections can add significantly to the overall processing burden. Several possibilities for speeding up the calculations were highlighted in the text. The optimization of the atmospheric compensation process to take advantage of multiprocessor computers provides the best possibility of reaching the goal of efficient processing of hyperspectral data cubes.

Acknowledgments

The authors wish to thank Gail Anderson at the Air Force Research Laboratory for making available versions of MODTRAN and FLAASH for our studies prior to their official release and the reviewers for their insightful comments. We also want to thank Carolyn Upham and Kris Farrar for their help with the data processing.

REFERENCES

1. G. Vane, R.O. Green, T.G. Chrien, H.T. Enmark, E.G. Hansen, and W.M. Porter, "The Airborne Visible/Infrared Imaging Spectrometer (AVIRIS)," *Rem. Sens. Environ.* **44** (2/3), 1993, pp. 127–143.
2. J.W. Boardman, "Precision Geocoding of Low-Altitude AVIRIS Data: Lessons Learned in 1998," *Proc. 7th Ann. JPL Airborne Earth Science Workshop*, JPL Publication 99-17, Pasadena, Calif.,1999, pp. 63–68.
3. L.J. Rickard, R. Basedow, E. Zalewski, P. Silvergate, and M. Landers, "HYDICE: An Airborne System for Hyperspectral Imaging," *SPIE* **1937,** 1993, pp. 173–179.
4. R.W. Basedow, D.C. Carmer, and M.E. Anderson, "HYDICE System, Implementation and Performance," *SPIE* **2480,** 1995, pp. 258–267.
5. E.P. Shettle and R.W. Fenn, "Models for the Aerosols of the Lower Atmosphere and the Effects of Humidity Variations on Their Optical Properties," *AFGL TR 79-0214*, Air Force Geophysics Lab., Hanscom AFB, Mass., 20 Sept. 1979.
6. E.J. McCartney, *Optics of the Atmosphere: Scattering by Molecules and Particles* (Wiley, New York, 1976).
7. W. Malkmus, "Random Lorentz Band Model with Exponential-Tailed S^{-1} Line-Intensity Distribution Function," *J. Opt. Soc. Am.* **57** (3), 1967, pp. 323–329.
8. B.-C. Gao, and A.F.H. Goetz, "Column Atmospheric Water Vapor and Vegetation Liquid Water Retrievals from Airborne Imaging Spectrometer Data," *J. Geophys. Res.* **95** (D4), 1990, pp. 3549–3564.
9. B.C. Gao, and Y.J. Kaufman, "The MODIS Near-IR Water Vapor Algorithm, Algorithm Technical Background Doc. ID: MOD05: Total Precipitable Water," NASA Goddard Space Flight Center, Greenbelt, Md., 1997.
10. Y.J. Kaufman and B.-C. Gao, "Remote Sensing of Water Vapor in the Near IR from EOS/MODIS," *IEEE Trans. Geosci. Rem. Sens.* **30** (5), 1992, pp. 871–884.
11. B.-C. Gao, Y.J. Kaufman, W. Han, and W.J. Wiscombe, "Removal of Thin Cirrus Path Radiances in the 0.4–1.0 μm Spectral Region Using the 1.375-μm Strong Water Vapor Absorption Channel," *Proc. 7th Ann. JPL Airborne Earth Science Workshop*, JPL Publication 97-21, Pasadena, Calif., 1998, pp. 121–130.
12. M.K. Griffin, S.M. Hsu, K. Burke, and J.W. Snow, "Characterization and Delineation of Plumes, Clouds and Fires in Hyperspectral Images," *SPIE* **4049,** 2000, pp. 274–283.
13. A.D. Roberts, Y. Yamaguchi, and R.P. Lyon, "Calibration of Airborne Imaging Spectrometer Data to Percent Reflectance Using Field Spectral Measurements," *Proc. Nineteenth Int. Symp. on Remote Sensing of Environment* **2,** *Ann Arbor, Mich., 21–25 Oct. 1985,* pp. 679–88.
14. J.E. Conel, R.O. Green, G. Vane, C.J. Bruegge, R.E. Alley, and B.J. Curtiss, "Airborne Imaging Spectrometer-2: Radiometric Spectral Characteristics and Comparison of Ways to Compensate for the Atmosphere," *SPIE* **834**, 1987, pp. 140–157.
15. F.A. Kruse, "Use of Airborne Imaging Spectrometer Data to Map Minerals Associated with Hydrothermally Altered Rocks in the Northern Grapevine Mountains, Nevada, and California," *Rem. Sens. Env.* **24** (1), 1988, pp. 31–51.
16. B.-C. Gao, K.B. Heidebrecht, and A.F.H. Goetz, "Derivation of Scaled Surface Reflectances from AVIRIS Data," *Rem. Sens. Environ.* **44** (2/3), 1993, pp. 165–178.
17. S.M. Adler-Golden, A. Berk, L.S. Bernstein, S. Richtsmeier, P.K. Acharya, M.W. Matthew, G.P. Anderson, C. Allred, L. Jeong, and J. Chetwynd, "FLAASH, A MODTRAN4 Atmospheric Correction Package for Hyperspectral Data Retrievals and Simulations," *Proc. 7th Ann. JPL Airborne Earth Science Workshop*, JPL Publication 97-21, Pasadena, Calif., 1998, pp. 9–14.
18. E. Vermote, D. Tanre, J.L. Deuze, M. Herman, and J.J. Morcrette, "Second Simulation of the Satellite Signal in the Solar Spectrum (6S): 6S User's Guide Version 2," NASA Goddard Space Flight Center, Greenbelt, MD, 1997.
19. A. Berk, L.S. Bernstein, G.P. Anderson, P.K. Acharya, D.C. Robertson, J.H. Chetwynd, and S.M. Adler-Golden, "MODTRAN Cloud and Multiple Scattering Upgrades with Application to AVIRIS," *Remote Sens. Environ.* **65** (3), 1998, pp. 367–375.
20. Y.J. Kaufman and C. Sendra, "Algorithm for Automatic Atmospheric Corrections to Visible and Near-IR Satellite Imaging," *Int. J. Rem. Sens* **9** (8), 1988, pp. 1357–1381.
21. M.W. Matthew, S.M. Adler-Golden, A. Berk, S.C. Richtsmeier, R.Y. Levine, L.S. Bernstein, P.K. Acharya, G.P. Anderson, G.W. Felde, M.P. Hoke, A. Ratkowski, H. Burke, R.D. Kaiser, and D.P. Miller, "Status of Atmospheric Correction Using a MODTRAN4-Based Algorithm," *SPIE* **4049**, 2000, pp. 199–207.
22. S.M. Adler-Golden, M.W. Matthew, L.S. Bernstein, R.Y. Levine, A. Berk, S.C. Richtsmeier, P.K. Acharya, G.P. Anderson, G. Felde, J. Gardner, M. Hoke, L.S. Jeong, B. Pukall, J. Mello, A. Ratkowski, and H.-H. Burke, "Atmospheric Correction for Short-Wave Spectral Imagery Based on Modtran4," *Proc. 7th Ann. JPL Airborne Earth Science Workshop*, Pasadena, Calif., JPL Publication 97-21, pp. 9–14.
23. S.M. Adler-Golden, R. Y. Levine, A. Berk, L.S. Bernstein, G.P. Anderson, and B. Pukall, "Detection of Cirrus Clouds at 1.13 μm in AVIRIS Scenes over Land," *SPIE* **3756,** 1999, pp. 368–373.

MICHAEL K. GRIFFIN
is a staff member in the Sensor Technology and System Applications group. His current research focuses on applications of hyperspectral technology to meteorological and environmental applications. A recent effort involved the design and employment of a cloud cover detection algorithm for the Hyperion hyperspectral sensor to run onboard the Earth Observer (EO)-1 space-based platform. He came to Lincoln Laboratory in 1997 to work on data analysis, algorithm development, and assessment of hyperspectral sensors. Prior to joining Lincoln Laboratory he was an atmospheric physicist at the Air Force Research Laboratory where he was involved in the development of cloud algorithms from multispectral imagery and worked on the retrieval of humidity, precipitation, and surface properties from microwave sensor measurements. He received a B.S. degree in physics and mathematics from California State University, Chico, and M.S. and Ph.D. degrees in meteorology from the University of Utah.

HSIAO-HUA K. BURKE
leads the Sensor Technology and System Applications group at Lincoln Laboratory. In the area of remote sensing, she specializes in applications of optical sensors, particularly data analysis and algorithm development. A recent area of interest is the application of hyperspectral technology to Department of Defense needs, including fusion of hyperspectral data information with other sensors. She received her Ph.D. degree in atmospheric physics from Rice University, and joined Lincoln Laboratory as a staff member in 1981.